Proceedings of the ASME 2010 3rd Joint US-European Fluids Engineering Summer Meeting and 8th International Conference on Nanochannels, Microchannels, and Minichannels
FEDSM-ICNMM2010
August 1-5, 2010, Montreal, Canada

FEDSM-ICNMM2010-30267

LARGE EDDY SIMULATIONS OF TAYLOR-GÖRTLER INSTABILITIES IN TRANSITIONAL AND TURBULENT BOUNDARY LAYERS

Sergej Gordeev
Karlsruhe Institute of Technology
Karlsruhe·Germany

Robert Stieglitz
Karlsruhe Institute of Technology
Karlsruhe·Germany

Volker Heinzel
Karlsruhe Institute of Technology
Karlsruhe·Germany

ABSTRACT

Free surface liquid metal targets are considered in several high power targets as a tool to produce secondary particles, since their power density exceeds material sustainable limits. Many target designs consider due to the high power deposited in the liquid a concave formed back plate in order to yield a higher boiling point. Upstream the free surface target domain the liquid metal flow is conditioned by a nozzle. However, a back-wall curvature as well as a concave shaped exit nozzle contour can lead to the occurrence of secondary motions in the flow caused by Taylor-Görtler (TG) instabilities. These motions may impact the hydrodynamic stability the flow and also lead to an undesired heat transfer from the hottest region produced within the liquid target towards the uncooled back plate.

In this study, the suitability of the Large Eddy Simulation (LES) technique to simulate the formation, development and destruction TG instabilities in transitional and turbulent boundary layers was tested by comparing the simulation results with experimental data reported in literature. All comparisons exhibit a qualitative and quantitative good agreement between experimental data and numerical predictions regarding the mean flow parameters and unsteady large-scale structures caused by TG instabilities.

1. INTRODUCTION

High velocity free-surface liquid lithium operated targets find application in many high-power accelerator facilities to remove safely the beam energy deposited within a continuum (e.g., IFMIF, [1]; FRANZ, U. Ratzinger et al., [2]; FAIR, [3]). One example is the target of the International Fusion Materials Irradiation Facility (IFMIF), which is an accelerator based deuteron-lithium neutron source to simulate a neutron irradiation field similar to that of a future fusion power reactor. Therein, the liquid lithium free surface of the target is located within the beam tube in a vacuum atmosphere. In order to generate a radial pressure distribution within the lithium layer, preventing the liquid from boiling at the interface, a concave shaped back plate is the considered as the preferred design option, which is sketched in fig. 1. The wall normal thickness of the lithium film is chosen in such a manner, that the

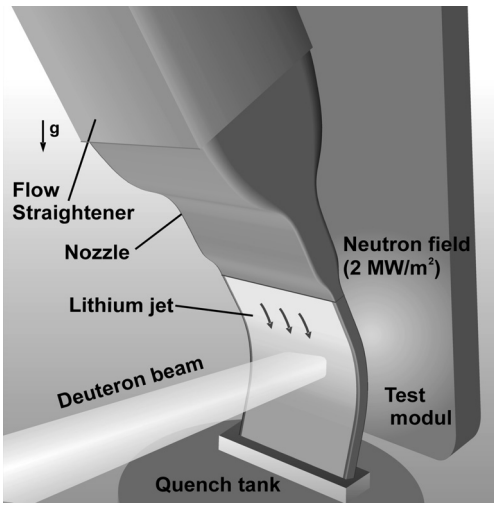

Figure 1. IFMIF liquid metal target

volumetric heat deposited by the particle beam does not penetrate into the back plate wall.

Before entering the target domain the lithium flow is conditioned by a nozzle, which has to form a lithium jet with a uniform velocity profile and low turbulence intensity at its exit. Both, the concave shaped nozzle wall as well as the back-wall curvature can lead to the appearance of secondary flow motions within the lithium flow caused by Taylor-Görtler (TG) instabilities.

The TG vortices appear in a quasi-steady manner as longitudinally along the flow direction arranged rolls with an extension normal to their axis of the size of the boundary layer, which is depicted schematically in fig. 2. TG-vortices occur due to the imbalance between of centrifugal forces and radial pressure gradients in transitional and turbulent boundary layer flow along a concave surface. The presence of TG vortices alters preliminary two-dimensional boundary layer flow into three-dimensional one, resulting in spanwise variation of

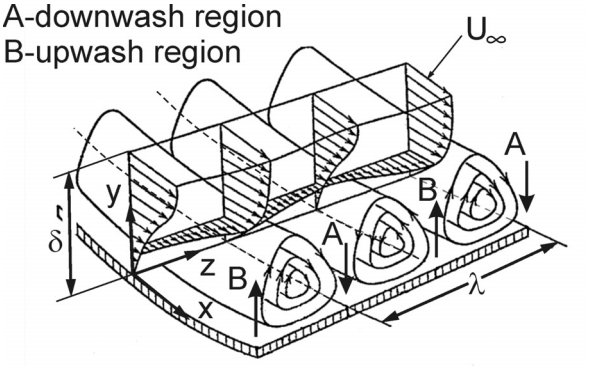

Figure 2: Sketch of the flow motions and variables describing Görtler instabilities

"upwash" regions where low momentum fluid moves away from the wall and "downwash" regions where high speed fluid moves towards the wall. The consequence of this macroscopic redistribution of mass is the development of mushroom shaped structures with strong inflection type velocity profiles in the normal (x) and spanwise (z) direction. A number of flow visualization studies (Jeans and Johnston, [4], Tani, [5]) show the spanwise variation of the mean velocity in a concave turbulent boundary layer caused by large-scale roll cells. These roll cells are produced by the same type of centrifugal instability mechanism that leads to the formation of TG vortices in the laminar boundary layer along a concave wall. As confirmed by experimental investigations, TG instabilities may potentially develop in accelerated flows close to concave walls. Takagi et al. [6]) observed the development of TG vortices on the concave walls and their dissipation in a contracted wind tunnel by a strongly accelerated flow.

The existence of TG vertices can promote a laminar-turbulent transition of the laminarized boundary layer within the nozzle flow, which further downstream may cause an irregular flow separation at the nozzle edge. Such kinds of motions can significantly impact the hydrodynamic stability of the jet flow and the heat transfer from the hottest region in the target, which is located within the flowing lithium, to the back plate, which in turn may then exceed material sustainable limits. In case of targets where the boundary layer thickness is of order of the wall normal lithium film depth TG vortices can affect the stability of the free surface considerably. The opaqueness of the liquid metal allows hardly to observe vortices in the nozzle or at the back plate. Therefore, this paper deals with the validation of simulation tools in order to predict or exclude reliably the existence of vortices and their impact on the flow stability.

In general turbulent fluid flow computations based on Reynolds-averaged models are not capable to predict this kind of vortices and must resort to ad hoc correction terms (see the review of Patel and Sotiropoulos, [7]). In contrast to Reynolds-averaged approaches, the Large Eddy Simulation (LES) is well suited for the simulation of the turbulent concave wall boundary layer flow, since the TG vortices are simulated directly.

2. VALIDATION CASES AND COMPUTATIONAL DOMAINS

Unfortunately no experimental data with flow conditions, which are fully consistent with the liquid-metal target operation conditions, are available.

Therefore, the suitability of the LES technique for the simulation of the formation and development of TG vortices in the transitional and turbulent boundary layers has been validated using three different sets of experiments, where several effects, accompanied the development of TG instabilities in the liquid-metal target flow, are presented.

The simulations have been performed by means of the wall-adapting local eddy-viscosity (WALE) Subgrid-Scale (WSG) model, proposed by Nicoud and Ducros [8] and offered by the CFD code Star-CCM+ [9]. Unlike the Smagorinsky model [10], the WSG model takes into account both the effects of strain and rotation rates. Additionally, the WSG model is suitable for the simulation of transitional flows.

First experiment conducted by Swearingen and Blackwelder [11] considers a boundary layer in a curved 2440 mm long test section, which has a cross section of 1200x150mm and a radius of curvature of 3200 mm. Measurements were performed in the air flow at a mean free stream velocity of U_∞=5m/s corresponding to variations of Re_x from 10^4 to $4x10^5$. Numerically the test section is modelled by $2x10^6$ fluid cells as shown in fig. 3. In the spanwise direction (z), the domain extends approximately eight boundary layers and has periodic boundary conditions.

The ability of the LES technique to predict the development of TG vortices in the accelerated boundary layer has been tested on the experimental data of Takagi et al [6]. In contrast to the case 1, the destabilizing influence of the nozzle wall curvature interacts with the stabilizing effect of the

acceleration. The contraction curve of the nozzle with a streamwise length of 1800 mm was designed by 6th order polynomial with an area contraction ratio of 9:1. The free stream velocity U_∞ at the nozzle exit was varied from 5 to 65 m/s corresponding to $1.25\text{x}10^6 \leq Re_x \leq 5.6\text{x}10^6$. In this Reynolds number range it is assured that within the nozzle the acceleration parameter K_{acc} exceeds at some local position x the critical value of $K_{acc}=3.0\text{x}10^{-6}$.

For this geometric set-up a half of the nozzle has been modelled as illustrated in figure 4 taking advantage of symmetry conditions. Since TG instabilities appear close to the contraction wall within the boundary layer far from the symmetry plane, the impact of the symmetry condition on the turbulence is negligibly small.

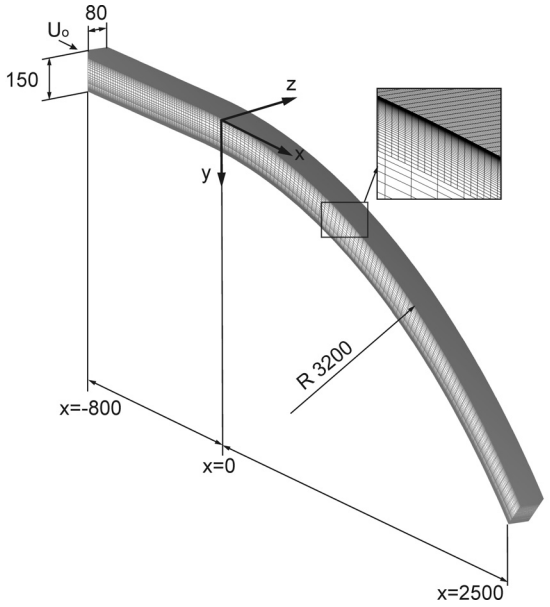

Figure 3: Computational grid of the test section from Swearingen at al. [8]

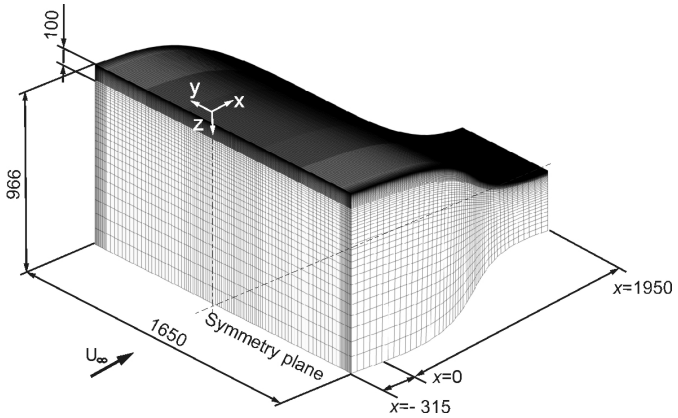

Figure 4: Computational grid of the contraction nozzle from Takagi at al. [9]

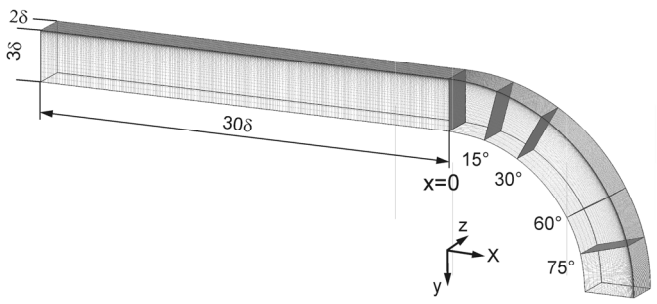

Figure 5: Computational grid for the test section from Barlow and Johnston [10]. Flat channel dimensions are related to the boundary layer thickness at the beginning of the curved part δ=75 mm.

The investigated area in the middle of the upper contraction wall has dimensions of twice the wall normal boundary layer thickness and about ten times its thickness in spanwise (y) direction. The grid generated within the investigated area consists of 400x50x250 grid points in streamwise (x), wall-normal (z) and spanwise directions, respectively.

In both cases the mean velocity shape at the inlet is laminar. The mean velocity profiles at the inlet are interpolated from the experimental data and slightly perturbed with the random-flow-generation procedure. At the exit, pressure outlet conditions are used.

In the third test case the simulation attempts to reproduce the laboratory experiments conducted by Barlow and Johnston [12]. The experimental facility is a water channel where a straight entry flow section is fitted to a 90° constant radius (R=1360 mm) curved bend. Measurements have been conducted only for the concave wall. The water flows down a 4880 mm long, straight section at a nominal velocity of 0.15 m/s and becomes fully turbulent at the beginning of the curved channel part at x=0. The boundary layer thickness at the start of the curvature is about δ=75 mm and has a momentum thickness Reynolds number of about $Re_{\delta 2}$=1300. The test section has been modelled using $2.1 \cdot 10^6$ fluid cells. The number of grid points within the boundary layer in the span wise and wall-normal directions is 81 and 51, respectively. The calculation begins approximately 30 boundary layer thicknesses upstream of the curved section and ends at the 90° position. The domain extends two boundary layer thicknesses in spanwise direction and periodic boundary conditions are used. In this case, time-depended inflow boundary conditions are required to ensure that the boundary layer is fully turbulent at the beginning of the curved part. In the present study the random-flow-generation (RFG) technique of Smirnov et al. [13] is employed.

In all the cases, the grid cells are clustered near the wall, so that the first cell layer falls within the viscous sublayer $y^+<5$. It is important that the resolved turbulent scales have to be in the inertial region of the turbulent kinetic energy spectrum. According to Baggett et al. [14], the grid filter (Δ) should be at

least one-tenth of the larger scales ($L_\varepsilon=k^{3/2}/\varepsilon$). In addition to the larger scales and filter width, Taylor ($\lambda=(10\nu k/\varepsilon)^{1/2}$) and Kolmogorov ($\eta=(\nu^3/\varepsilon)^{1/4}$) scales are also computed to reveal where the grid filter is located amongst the turbulent length scales. Computations of these scales are performed using the v^2f-model proposed by Durbin [15]. The grid filter in the boundary layer area generally lies in between the larger scales and the Taylor scales, but much closer to the Taylor scales. The grid sensitivity tests showed that there is no significant variation between the results for the present and refined grid resolutions. The time step Δt employed for the predictions corresponds to a Courant number Co less than 0.5.

3. RESULTS AND DISCUSSION

3.1 Test case 1

For case 1 the calculation accuracy has been quantified by comparing the growth of the vortex system of the measurements and the calculation. Figure 6 shows contours of the normalized stream wise velocity U/U_∞ in the channels cross section for different stream wise positions. The calculation results show a good agreement with experiments for the development of TG vortices. At the position of 80cm downstream the inlet both measurements and calculations indicate the growth of vortex structures expressed by a thickening of the boundary layer in the up-wash region. Further downstream at the position of x=100cm, the effects of the stream wise vorticity become more and more pronounced. The vortices grow in wall-normal direction and reach a size of approximately twice the Blasius boundary layer thickness. The simulation exhibits a good agreement with the experiments in predicting the spanwise wave length (approximately 18-20 mm). Downstream at x=110cm the spanwise structure starts decaying due to an enhanced mixing and the onset of a developed turbulent flow.

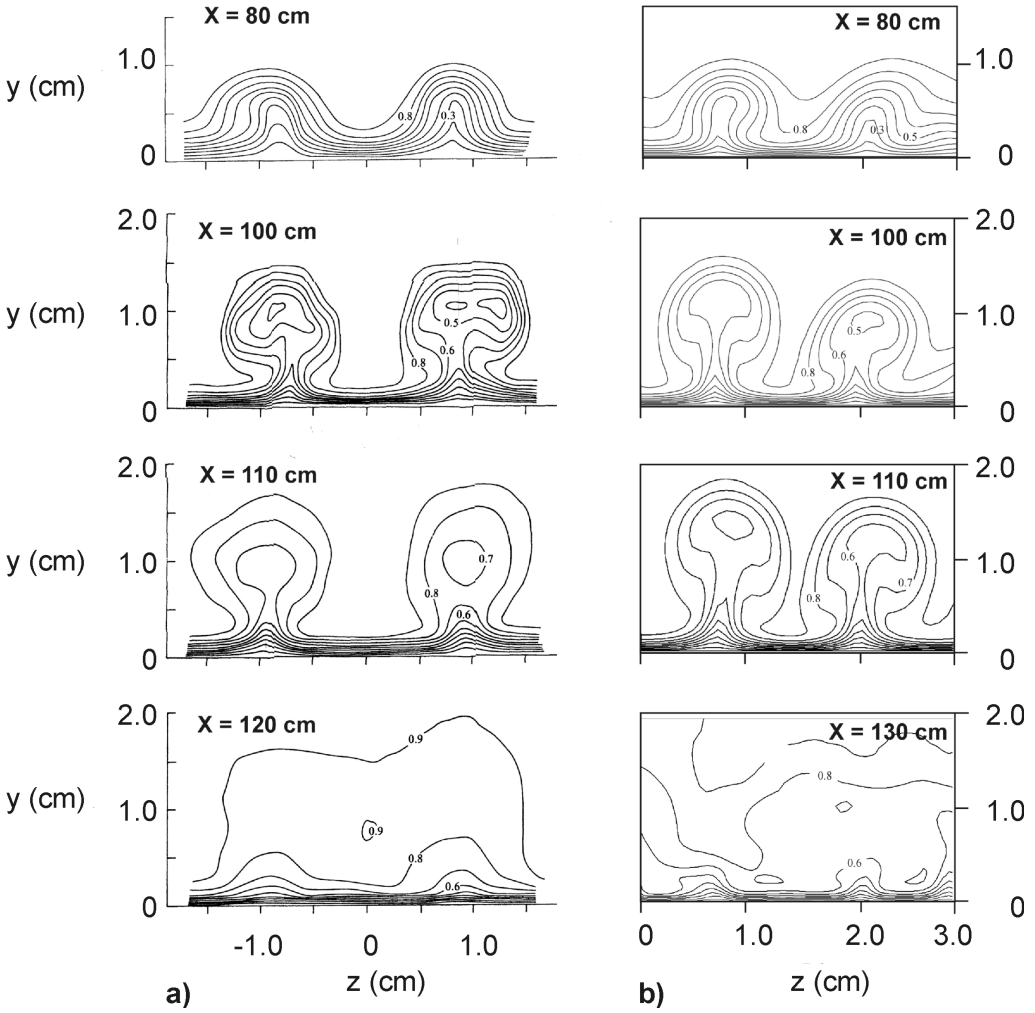

Figure 6: Calculated normalised streamwise velocity contours U/U_∞ (b) compared with experimental data [11] (a) in different downstream wall normal planes.

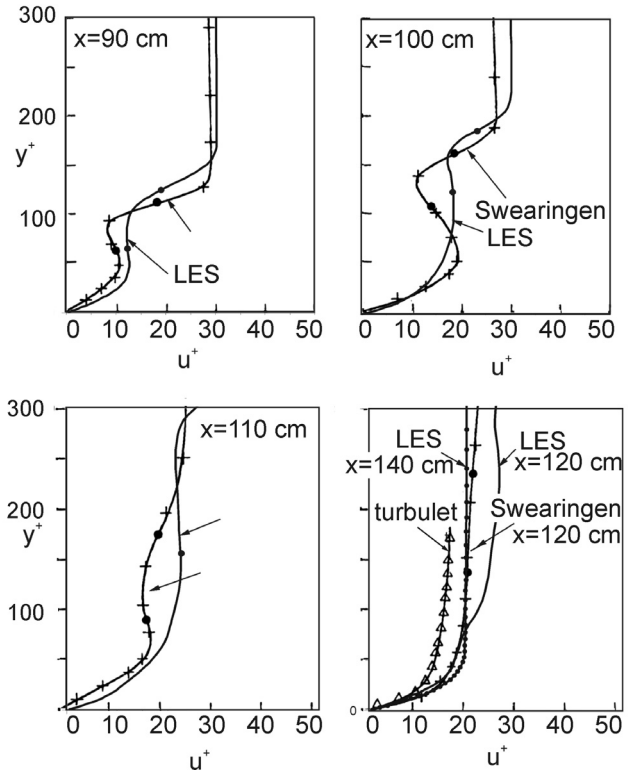

Figure 7: Calculated dimensionless mean streamwise velocity profiles u^+ (=U/u_τ) as a function of dimensionless wall distance y^+ (=yu_τ/ν) at the center of a single low-speed region compared with measurements [11] in different downstream wall normal planes *x*.

Figure 7 compares the measured and computed nondimensional velocity $u^+(=U/u_\tau)$ as a function of the wall normal non-dimensional distance y^+ at different axial positions x. The pumping action of the counter-rotating vortices gradually generates an S-shaped velocity profile with two inflection points (black points in fig. 7) in regions of intense local horizontal shear layers. The WSG model reproduces the development of a S-shaped profile and thus the generation of the vortex system with an acceptable qualitative and quantitative agreement with the experimental data

3.2 Test case 2

Related to the Takagi experiment [6] in the contraction nozzle the fig. 8 compares for U_∞=10.5m/s the measured and the calculated streamwise evolution of the normalized mean (U/U_∞) and the dimensionless fluctuating (u'/U_∞) velocity components along the contraction. The comparison shows the ability of the WSG model to predict in a reasonable agreement with the experimental observation the evolution of the boundary layer velocity shape along the curved contraction nozzle. Near the inlet (x/L=0.085 and x/L=0.1), the WSG model underestimates the flow separation. The reason for this discrepancy can be related to the differences between inflow conditions of experiment and computation. In agreement with measurements the WSG model shows the distortion of the velocity profile and the increase of the turbulence level on the contraction length between x/L=0.1 and x/L=0.6. Further downstream within the convex part the boundary layer is thinned and laminarized by the acceleration, as depicted in fig. 8 at the positions x/L=0.58 and 0.85. Also here, the qualitative changes of the profiles with the decay of the turbulence intensity are well reproduced by the simulation.

Figure 9a illustrates the vortex motion within the boundary layer in the plane normal to the flow in the contraction at x/L=0.21, which is conducted by means of a light sheet using smoke injected upstream. In order to visualize the mass transport in the vertical structures a passive scalar with the same characteristics as air is injected at the inlet close to the contraction wall. Figure 9b shows the computed concentration field of the passive scalar in the boundary layer cross section in the same plane (x/L=0.21). In both pictures, several pairs of counter rotating streamwise vortices with a mushroom-like shape can be easily identified. Similar to the experimental observations, the strength of the vortices is not even, some roll-up motions are suppressed by neighbouring vortices. A possible explanation is the influence of the wall normal contraction (z) causing a change of the boundary layer thickness and hence

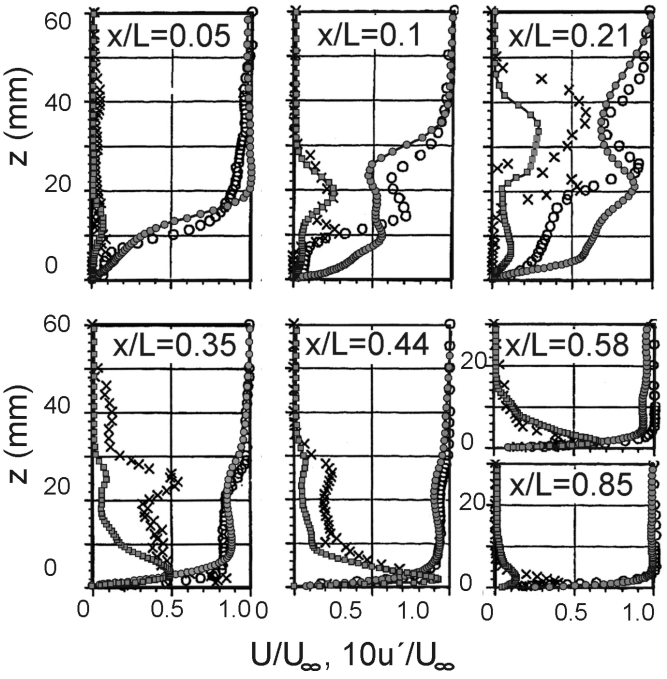

Figure 8: Comparison of measured [6] and calculated streamwise variation of the mean velocity (U/U_∞) and fluctuating velocity (u'/U_∞) profiles in the middle of upper nozzle wall at different axial positions *x/L*.

Experiment: ○ U/U_∞, x $10u'/U_\infty$;

LES: —●— U/U_∞, —■— $10u'/U_\infty$

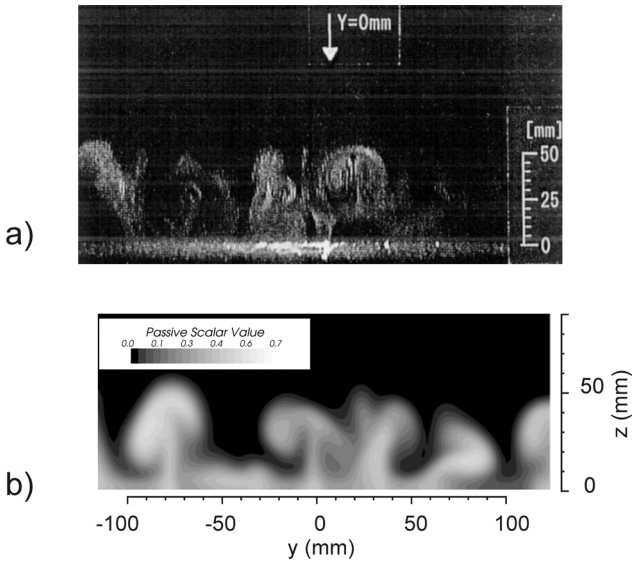

Figure 9 a) Smoke visualization of vortex motions in the boundary layer in the plane normal to the contraction wall at *x/L*=0.21 (from [6]); b) Calculated instantaneous concentration field of the passive scalar in the boundary layer at *x/L*=0.21.

yielding the appearance of a wall normal velocity component near the contraction wall. Another factor altering the vortex structure is the contraction in the spanwise direction (y). Additionally, secondary flows induced by pressure gradients in transverse direction can effect the development of the TG structures.

3.3 Test case 3

3.3.1 Time averaged profiles

In the figures 10 the non-dimensional mean velocity profiles u^+ at several streamwise positions are compared with experimental data.

The first position is located within the flat part of the section (x=600 mm), the next four ones are at 15°, 30° and 60° (or at x=356, 712 and 1424 mm from the start of the curved section; see cf. nomenclature of figure 5). The graphs show that the agreement between simulation and experiment is quite good independent of what position is looked at. Both, in experiment and simulation the boundary layer can be considered to be composed of two layers, an inner region ($y^+ < 50$) where the profiles match the universal u_τ scaling, and an outer one where the mean velocity profile under influence of concave curvature deviates from the logarithmic law and remains below it out to the free stream. A minor disagreement with measurements is observed at 15°. There, the experimental data of the velocity profile at 15° are closer to a flat profile and the change in the profile shape between 15° and 30° is more pronounced than in the simulation. The reason for this discrepancy can be explained with the slight variation of the channel height in the curved test section, which was not taking into account in the simulation.

The computed streamwise and normal velocity fluctuations are compared with the experiments in fig. 11. Figure 11a shows the streamwise velocity fluctuations profiles $\sqrt{(u')^2}/U_p$ of the outer-layer ($\delta\approx1$) at the flat (x=-880 mm) and curved (60°) positions. The turbulence intensity data are normalized with the inviscid velocity U_p that would be achieved at the wall. The agreement with the experimental data is acceptable and the qualitative change of the profile resulting from a concave curvature is well reproduced. On the quantitative level, the streamwise fluctuation on the flat station is slightly overpredicted by 10% in the region $0.4<y/\delta<0.8$. The reason for this discrepancy is not clear, but it can be related to the differences in the inflow conditions in experiments and simulations.

Figure 11b shows profile of wall-normal velocity fluctuations $\sqrt{(v')^2}/U_p$. Once again, simulations results have a good qualitative agreement with experimental data. As expected, changes in v' are more pronounced. The peak value of v' increases by about 50% between the flat and 60° stations, and the location of the peak moves from $y/\delta\approx0.2$ to $y/\delta\approx0.4$. On a quantitative level, the peak of the v' at 60° station is slightly overpredicted by about 6%.

3.3.2 Visualization of the instantaneous flow.

In experiments the structures generated in the flat and concave boundary layers are visualized by means of the Laser-Induced-Fluorescence (LIF) technique. Figures 12 include LIF photographs of the boundary layer with different exposure times. The laser sheet was positioned at two streamwise locations: on the flat wall at x=-120 mm and on the curved wall at 60°, with dye being injected 600 mm upstream of each position. The 0.01s exposure exhibits an instantaneous picture of the flow organisation within the individual eddies. The 2 s exposure provides a short time average view of the flow, and the 60 s gives a relatively long temporal average, which can be interpreted as the integrated axial flow configuration. In simulation the dye is modelled as passive scalar with the same physical characteristics as water, which is injected at the same positions as in experiment. In the flat boundary layer, ejections of the dye marked fluid (fig 12a) as well as the concentration field of the passive scalar (figure 13a) shown in the 0.01 s exposure appear to be uniformly distributed in space and time. As result the longer exposures show relatively homogenous distribution of the dye and passive scalar.

The structure of the concave boundary layer is also predicted with relatively good accuracy. As shown in figure 13b for the exposure time 0.01 s the passive scalar is no longer uniformly distributed, as in case of the flat boundary layer, but it is rather concentrated into separate large scale outflows with a typical mushroom shape.

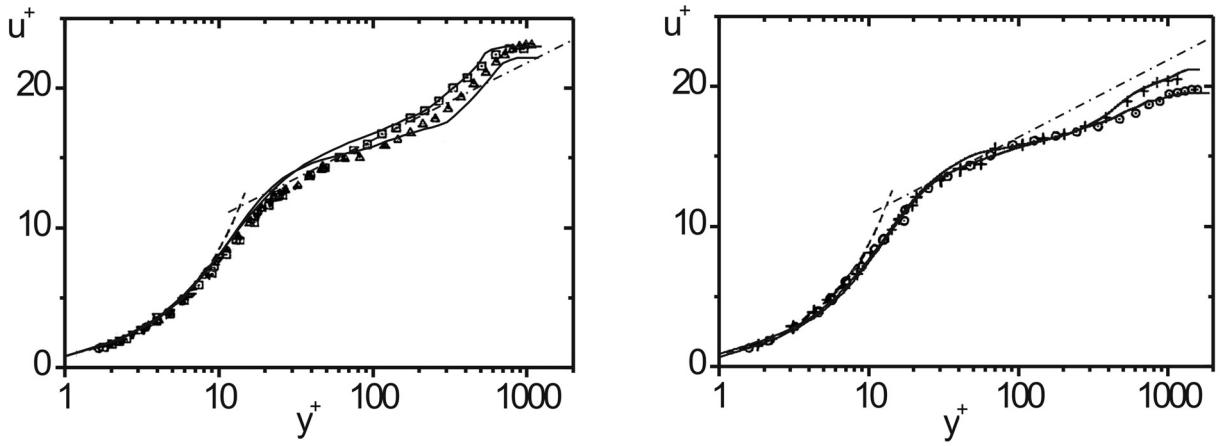

Figure 10. Streamwise non-dimensional mean velocity profiles u^+ vs. y^+ on the flat station (x=600mm) and on the curved test section at 15°,30°,60 respectively. Barlow and Johnston [12]: □, flat; Δ, 15°; +, 30°; ○, 60°; LES WSG: solid lines

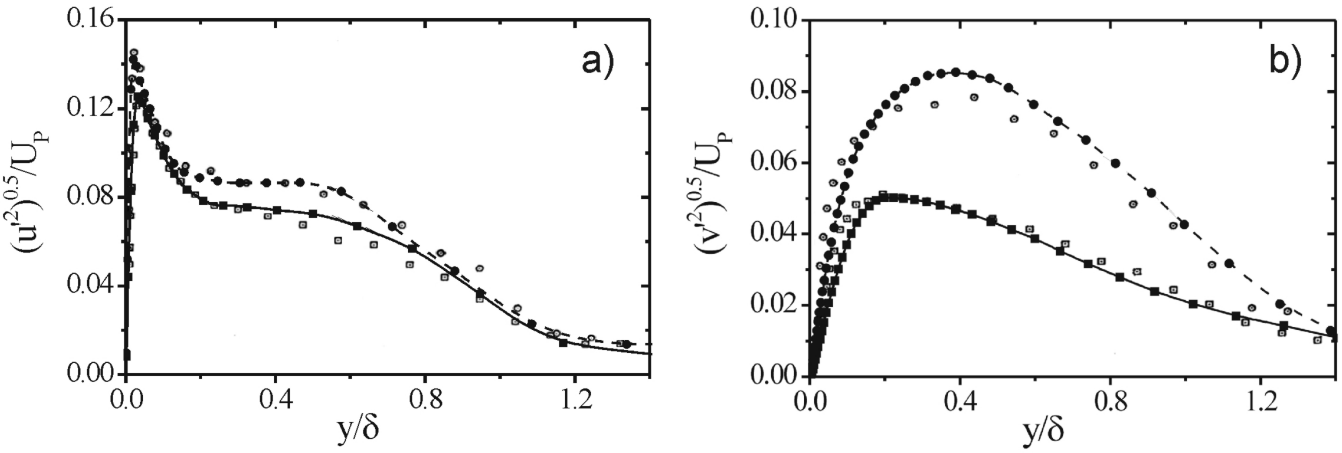

Figure 11. Streamwise turbulence intensity $\sqrt{(u')^2}/U_p$ (a) and wall-normal velocity fluctuation $\sqrt{(v')^2}/U_p$ (b) profiles measured in the boundary layer at the flat (x=-880 mm) and concave (60°) stations compared with simulation results. Barlow and Johnston [12]: □, flat; ○, 60°; LES WSG: —■—, flat; — ● —, 60°;

This proofs the existence of the streamwise vortex structures, which resemble TG vortices and are denoted by Barlow and Johnston "roll-cells". Corresponding to the experimental observations these structures do not have stationary spanwise locations. They are rather variable in space and time, with an average streamwise coherence of about four to five boundary layer thicknesses. Although in the short time average (2 s exposure) these structures are well visible, in a 60 s exposure their unsteady behaviour results in a relatively uniform image nearly completely hiding them.

In order to explore the structural characteristics and dynamics of the large-scale coherent vortices, their structural development and transformation during the transition from the flat to the concave boundary layer flow can be identified by a method based on the second invariant of the velocity-gradient tensor Q proposed by Hunt et al.[16]. In fig. 14, the large-scale vortices in the flat and concave boundary layer are visualized by plotting the iso-surface of Q=0.5. The iso-surface of the instantaneous streamwise velocity $U= 0.85U_\infty$ (dark gray) is also shown in the graph to signify regions of low-speed fluids. Figure 14a shows the zoomed fragment of the vortex structure in the flat boundary layer. Vortices in the outer region of the boundary layer ($100< y^+ <600$) are organized into packets, which are formed by 2 to 5 streamwise aligned hairpin or one-side cane-type vortices inducing a low-speed zones between their legs. The streamwise alignment of hairpin structures is consistent with the concept model of vortex organisation in the turbulent boundary layer found by Adrian et al. [17].

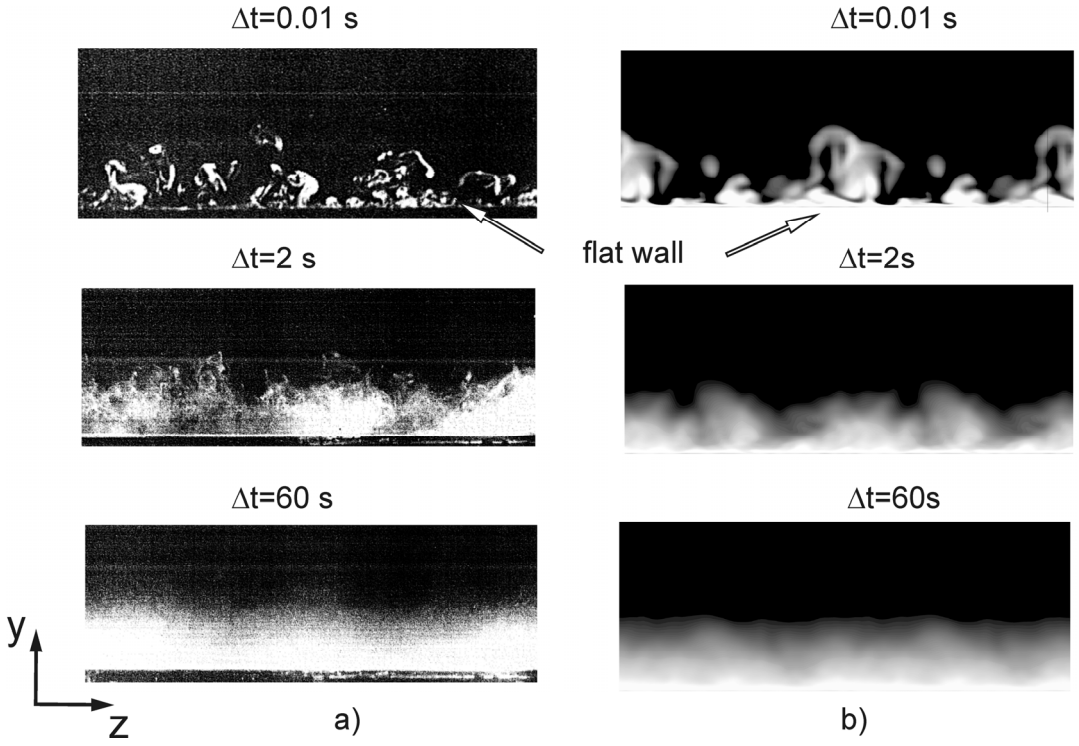

Figure 12. Laser induced fluorescence photographs with different exposure times showing the (*y*-*z*)-plane in the flat boundary layer flow with dye at *x*=-120mm (a) compared with calculated concentration oft the passive scalar (b) injected at the same positions as in experiment.

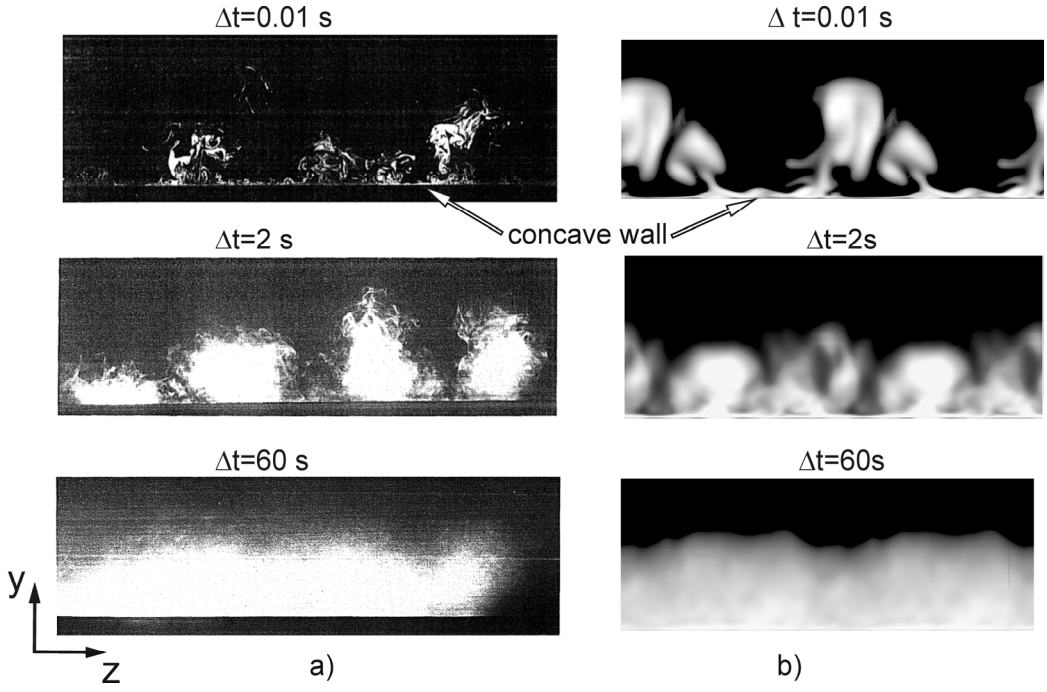

Figure 13. Laser induced fluorescence photographs with different exposure times showing the (y-z)-plane in the concave boundary layer flow at the 60° station (a) compared with calculated concentration oft the passive scalar (b)

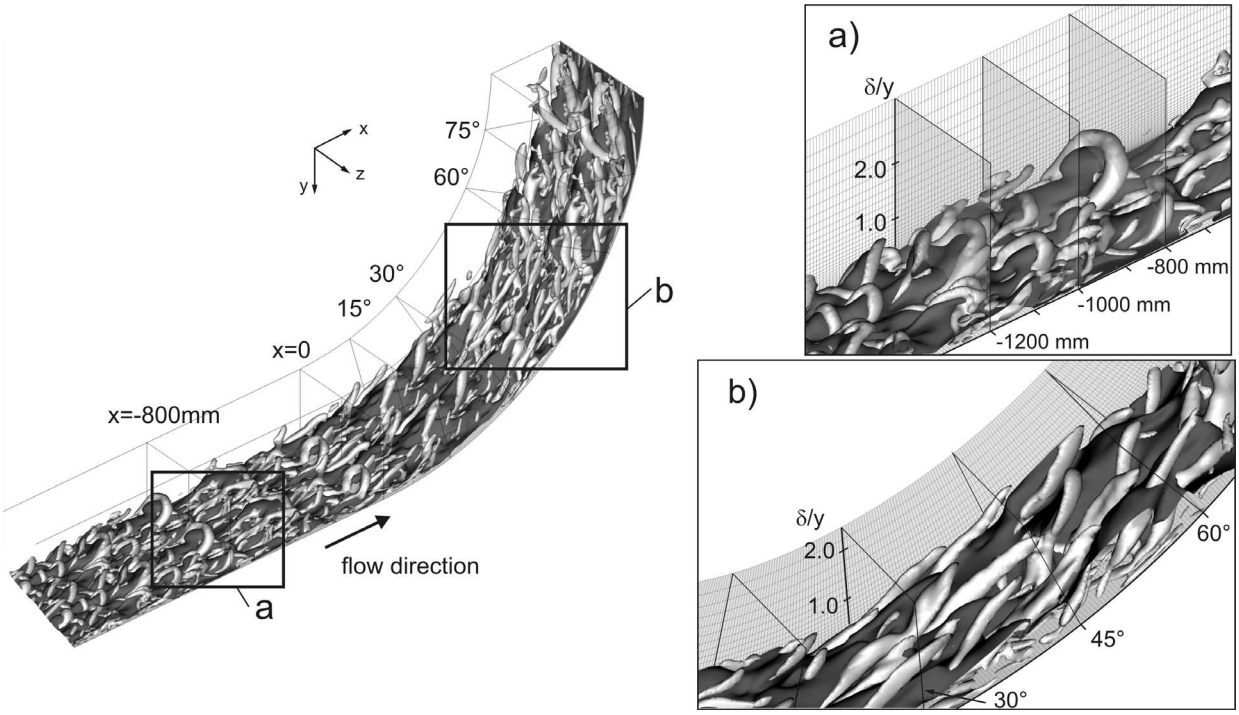

Figure 14. The iso-surfaces of instantaneous flow structures in the boundary layer flow determined by *Q*-criterion (*Q*=0.5) and of the instantaneous streamwise velocity $U = 0.85U_\infty$ (dark gray)

They concluded based on planar PIV measurements, that these packets are the dominant flow structure from the outer edge of the buffer layer to the outer wake region at each Reynolds number. In a good agreement with experimental observations hairpin vortices have the streamwise length variation from 1 to 3δ and the spanwise spacing 0.5 to 1δ. From beginning of the concave wall (fig. 14b), the centrifugal instability mechanism amplifies the intensity of the large–scale motions normal to the wall and significantly affects the turbulent structure. As a result, the increased shear stretches and intensifies the vortices along the streamwise direction. The flow acceleration in the vortex core suppresses the curl-up process between hair-pin vortex legs. The hairpin vortices are stretched in streamwise direction, the front part of the hair-pin narrows in the middle and the structure splits up in a streamwise aligned vortex pair, which length at 60° reaches up to 5 boundary layer thicknesses. The vortex pairs concentrate in banded cells inducing unusually long low-speed zones. In spite of the random character, newly organized structures have a long coherence compared with flat plate structures.

4. CONCLUSIONS

Analysis of liquid lithium operated targets exhibits that TG instabilities in the boundary layer flow within the nozzle as well as on the curved back plate likely occur during the nominal operation. They may affect the target performance considerably and hence demand a detailed investigation.

In order to quantify the magnitude of this aspect an LES WSG model has been set-up. Its validation process presented here is based on three well described experiments in literature.

First experiment has been conducted in a curved test section with the transitional air flow with zero pressure gradients. The LES WSG model reproduces the development of a S-shaped profile and thus the generation of the vortex system with an acceptable qualitative and quantitative agreement with the experimental data. The simulation exhibits a good agreement with the experiments in predicting the streamwise and spanwise wave length of the structures.

In the second test case the ability of the LES technique to predict the development of TG vortices in the accelerated boundary layer has been investigated. The comparison shows the ability of the WSG model to predict the behaviour of the accelerated boundary layer on a curved wall of the nozzle contraction correctly. In agreement with measurements the WSG model shows the distortion of the velocity profile and the increase of the turbulence level on the concave wall. The qualitative change of the boundary layer accompanied with the decay of the turbulence intensity within the convex nozzle part is also well reproduced.

The last simulation reported in the paper attempt to reproduce a laboratory experiments with a fully developed turbulent water flow over flat and concave walls. The simulation results accurately reproduce the structural changes in the turbulent boundary layer during the transition from a flat

wall to a concave shaped wall. In agreement with experimental observations, the visualization of predicted large-scale vortex structure in the boundary layer shows the reorganization of typical flat-plate hair-pin structures in long coherent streamwise aligned vortex cells along the concave surface. Some discrepancies between the predictions and experimental data can be attributed to the grid resolution, but also to the incomplete inflow data and the experimental uncertainties.

With respect to the article presented in this context the WSG based LES simulation is considered to be validated in terms of capturing TG vortices in conventional liquids. In the next step this technique will be transferred to predict the performance of nuclear liquid metal targets for which unfortunately no broad extended experimental data are available.

NOMENCLATURE

Nomenclature

Co	Courant number $=\Delta t\, U_\infty/\Delta x$
K_{acc}	acceleration parameter $= \left(\nu/U_\infty^2\right)\left(dU_\infty/dx\right)$
k	turbulent kinetic energy
L_ε	larger turbulent length scale $=k^{3/2}/\varepsilon$
Q	vortex identification criterion
R	radius
Re_x	Reynolds number $= x\, U_\infty/\nu$
$Re_{\delta 2}$	Reynolds number $= \delta_2\, U_\infty/\nu$
t	time
U,u	streamwise velocity
U_∞	mean velocity outside the boundary layer
u^+	nondimensional velocity $=U/u_\tau$
u_τ	friction velocity $=(\tau_w/\rho)^{0.5}$
V,v	normal velocity
x,y,z	Cartesian coordinates,
y^+	nondimensional wall distance $= y\, u_\tau/\nu$

Greek Symbols

Δ	filter width
δ	boundary layer thickness
δ_2	boundary layer Momentum thickness
λ	Taylor length scale$= (10\nu k/\varepsilon)^{1/2}$
η	Kolmogorov length scale$= (\nu^3/\varepsilon)^{1/4}$
ε	turbulent dissipation
ν	kinematic viscosity
τ_w	wall shear stress

Superscripts

$'$	fluctuating value

ACKNOWLEDGMENTS

The authors would also like to thank Prof. Dr. U. Müller for the fruitful discussions during the conductance of this work.

REFERENCES

1. IFMIF Comprehensive design report. The International Energy Agency, 2004.
2. U. Ratzinger, L. P. Chau, O.L. Meuse, A. Schempp, K. Volk, M. Heil, F. Käppeler and R. Sieglitz. Intense pulsed neutron source FRANZ in the 1 – 500 keV Range, 18th Meeting of the International Collaboratorium on Advanced Neutron Sources, April 25-29, 2007, Guangdong, China.
3. An International Accelerator FAIR, Conceptual Design Report, 2001; http://www.gsi.de/GSI-Future/cdr/.
4. H. Jeans and J. P. Johnston., The effect of concave curvature on turbulent boundary layer structure. Rept. MD-40, Thermoscience Div.; Dept. of Mech. Eng.; Stanford University, 1982.
5. Tani, Production of longitudinal vortices in the boundary layer along a concave wall. J. Geophys. Res. 67, 3075–3080, 1962.
6. S. Takagi, A. Nishizawa and N. Tokugawa, Observation of Görtler vortices in wind-tunnel contraction boundary layer. In Third International Symposium on Turbulence, Heat and Mass Transfer (Edited by Y. Nagano, K. Hanjalic and T. Tsuji), pp. 275-282, 2000.
7. V.C. Patel and F. Sotiropoulos, Longitudinal curvature effects in turbulent boundary layers, Prog. Aerospace Sci. 33 (1997), pp. 1–70.
8. F. Nicoud, F. Ducros, Subgrid-scale stress modelling based on the square of the velocity gradient tensor. Flow, Turbul. Combust. 62 (3), 183–200, 1999.
9. STAR-CCM+ Version 4.02.011, CD adapco, 2008.
10. J. Smagorinsky, General circulation experiments with primitive equations. I. The basic experiment. Monthly Weather Rev. 91, 99, 1963.
11. J.D. Swearingen and R.F. Blackwelder, The growth and breakdown of streamwise vortices in the presence of a wall. J. Fluid Mech. 182, pp. 255-290, 1987.
12. Barlow R.S.; Johnston J.P. Structure of a turbulent boundary layer on a concave surface. J. Fluid Mech. 191, pp. 137–176, 1988
13. S. Smirnov, Shi and I. Celik, Random Flow Generation,Technique for Large Eddy Simulations and Particle-Dynamics Modeling. Trans. ASME. Journal of Fluids Engineering, 123, pp. 359-371, 2001.
14. J.S. Baggett , J. Jimenez, A.G. Kravchenko, Resolution Requirements in Large-eddy Simulations of Shear Flows, Annual Research Briefs. Center for Turbulence Research, Stanford University, Stanford, USA, 1997.
15. Durbin, P.A., Separated flow computations with the k-ε-v2 model, AIAA J. 33 (1995) 659-664.
16. J.C.R. Hunt, C.A.A. Wray and P. Moin, Eddies, Streams, and Convergence Zones in Turbulent Flows. Center for Turbulence Research Report CTR-S88, Stanford University, 193–207, 1988.
17. R. J.Adrian, C. D. Meinhart and C. D. Tomkins, Vortex organization in the outer region of the turbulent boundary layer. J. Fluid Mech. 422, 1–53, 2000.

